Bioactive Materials 24 (2023) 185–196

Contents lists available at ScienceDirect

Bioactive Materials

journal homepage: www.keaipublishing.com/en/journals/bioactive-materials

Pt(IV) prodrug initiated microparticles from microfluidics for tumor chemo-, photothermal and photodynamic combination therapy

Qingfei Zhang [a,b], Xiaocheng Wang [a,b], Gaizhen Kuang [a,b], Yuanjin Zhao [a,b,*]

[a] Department of Rheumatology and Immunology, Nanjing Drum Tower Hospital, School of Biological Science and Medical Engineering, Southeast University, Nanjing, 210096, China

[b] Oujiang Laboratory (Zhejiang Lab for Regenerative Medicine, Vision and Brain Health), Wenzhou Institute, University of Chinese Academy of Sciences, Wenzhou, 325001, China

ARTICLE INFO

Keywords:
Microfluidics
Hydrogel microparticle
Chemotherapy
Photothermal
Photodynamic
Cancer therapy

ABSTRACT

Multimodal treatment modalities hold great potential for cancer therapy, thus current efforts are focusing on the development of more effective and practical synergistic therapeutic platforms. Herein, we present a novel *trans, trans,trans*-$[Pt(N_3)_2(OH)_2(py)_2]$ (Pt(IV)) prodrug-initiated hydrogel microparticles (M_{ICG-Pt}) with indocyanine green (ICG) encapsulation by microfluidics for efficiently synergistic chemo-, photothermal (PTT) and photodynamic therapy (PDT). The employed Pt(IV) could not only serves as an initiator to generate azidyl radical ($N_3^{\bullet}$) for photo-polymerization of methacrylate gelatin (GelMA) matrix, but also be reduced to high cytotoxic platinum (II) (Pt(II)) species for tumor chemotherapy. The laden ICG with highly photothermal heating ability and intrinsic reactive oxygen species (ROS) productivity endows the M_{ICG-Pt} with effective PTT/PDT performances upon near-infrared (NIR) light irradiation. In addition, benefiting from the production of oxygen during the photo-activation process of Pt(IV), the PDT efficacy of ICG-laden M_{ICG-Pt} could be further enhanced. Based on these advantages, we have demonstrated that the M_{ICG-Pt} could significantly eliminate cancer cells *in vitro*, and remarkably suppressed the tumor growth *in vivo via* synergistic chemotherapy, PTT, and PDT. These results indicate that such Pt(IV)-initiated hydrogel microparticles are ideal candidates of multimodal treatment platforms, holding great prospects for cancer therapy.

1. Introduction

Cancer is one of the leading causes of death worldwide, which seriously threatens human health and life [1,2]. As a primary clinical treatment modality, chemotherapy uses cytotoxic chemical agents to directly eliminate cancer cells [3–6]. In this aspect, platinum-based drugs have been widely employed for treating a broad spectrum of malignant tumors, while their clinical application suffers from several drawbacks such as drug resistance and severe toxic side effects [7–12]. As an alternative, phototherapies, such as photothermal (PTT) and photodynamic therapy (PDT), have gained intensive attention owing to their minimal invasiveness, high spatiotemporal selectivity and controllability [13–18]. In particular, by combining phototherapies with traditional chemotherapy, various multimodal therapeutic systems have been developed based on polymers encapsulation, such as alginate, poly (lactic-*co*-glycolic acid), gelatin, cellulose, silk fibroin, and chitosan [19–23]. However, due to the lacking of elaborate design, most of these polymer-based systems not only require complicated and tedious preparation processes but also can hardly achieve multimodal therapeutic functions [24,25]. In addition, the polymerization of these systems commonly requires additional initiators, extra metal ions, and/or other crosslinkers, resulting in potential side effects in patients [26]. Thus, it is still highly anticipated to develop a facile multimodal therapeutic platform with simple structures but multiple functions for efficient synergistic chemo-, PTT and PDT.

In this paper, we present novel Pt(IV) prodrug-initiated photo-polymerized hydrogel microparticles (M_{ICG-Pt}) by using droplet microfluidics with the desired multiple functions for tumor combination therapy, as schemed in Fig. 1. Microfluidic technology with high precision and controllability has been widely used to prepare

Peer review under responsibility of KeAi Communications Co., Ltd.

* Corresponding author. Department of Rheumatology and Immunology, Nanjing Drum Tower Hospital, School of Biological Science and Medical Engineering, Southeast University, Nanjing, 210096, China.

E-mail address: yjzhao@seu.edu.cn (Y. Zhao).

https://doi.org/10.1016/j.bioactmat.2022.12.020

Received 31 October 2022; Received in revised form 9 December 2022; Accepted 20 December 2022

multifunctional microparticles or microcapsules for various biomedical applications including drug/cell delivery, cell culture, and tissue engineering [27–32]. Especially, the resultant microparticles or microcapsules with tunable sizes, dispersity, structures, and components could be employed as delivery systems of multimodal tumor therapy [33–36]. Although with many successes, the generation of most of these polymer microcarriers often requires additional extra initiators. In contrast, the photo-activatable platinum(IV)-azide complexes (Pt(IV) prodrugs) have been previously encapsulated in nano/microcarriers for tumor therapy due to its transformation to highly cytotoxic Pt(II) species [37–41]. During this photo-activation process, the $N_3^{\bullet}$ could also be generated from Pt(IV). Given the radicals triggered photo-crosslinking in many photo-cross-linkable hydrogels [42–44], we envision that the polymerization of these hydrogels could be initiated by $N_3^{\bullet}$. Besides, oxygen could also be generated during this process; which is crucial for ROS production by photosensitizers (PSs) [45,46]. Hence, it is conceivable that Pt(IV)-initiated polymerized microcarriers could be directly generated from microfluidic droplets without additional initiators and chemotherapeutic drugs, which simultaneously provides a versatile platform for loading PSs or photothermal agents (PTAs) to achieve the multiple functions for efficiently synergistic tumor therapy.

Herein, we fabricated the desired Pt(IV)-initiated photo-polymerized methacrylate gelatin (GelMA)-based hydrogel microparticles with indocyanine green (ICG) encapsulation *via* microfluidic electrospray for synergistic tumor chemotherapy, PTT, and PDT. A typical Pt(IV) of *trans, trans,trans*-$[Pt(N_3)_2(OH)_2(py)_2]$ was chosen not only as the prodrug generating high cytotoxic platinum(II) (Pt(II)) species for tumor chemotherapy but also as a novel initiator for the photo-polymerization of GelMA matrix to form the microparticles. ICG was encapsulated as PSs and PTAs in the microcarriers owing to its photothermal ability and ROS productivity for synergistic PTT/PDT under near-infrared (NIR) light irradiation. Besides, benefiting from the production of oxygen during the photo-activation process of Pt(IV), the PDT efficacy of the Pt(IV)-initiated ICG-laden microparticles ($M_{ICG\text{-}Pt}$) could be further enhanced. Based on these features, it was demonstrated that the $M_{ICG\text{-}Pt}$ displayed a significant killing effect on melanoma B16F10 cells *in vitro*, and substantially suppressed the growth of the melanoma and breast cancer model *in vivo via* synergistic chemotherapy, PTT, and PDT. These results indicate that such Pt(IV)-initiated hydrogel microparticles are ideal candidates for tumor multimodal therapy, representing an effective and versatile therapeutic platform for multiple biomedical applications.

2. Experiment section

2.1. Materials

Dipotassium tetrachloroplatinate (K_2PtCl_4) was bought from Platinum Energy. Co. Ltd, China. Pyridine (py), $AgNO_3$, NaN_3, and H_2O_2 (30%) were bought from Aladdin. Tryptophan (Trp), indocyanine green (ICG), 1,3-diphenylisobenzofuran (DPBF), and dimethyl pyridine *N*-oxide (DMPO) were bought from Macklin Inc. China. Calcein-AM/propidium iodide (PI) staining assay kit was bought from Meilunbio, Co., Ltd (Dalian, China). Tris(4,7-diphenyl-1,10-phenanthroline) ruthenium(II) dichloride ($[Ru(dpp)_3]Cl_2$) was bought from Bide Pharmatech Ltd (Shanghai, China). Hematoxylin and eosin (H&E) and Masson's trichrome staining kit were purchased from Solarbio Science & Technology Co., Ltd (Beijing, China). 2′,7-dichlorodihydrofluorescein diacetate (DCFH-DA), annexin V-FITC/PI apoptosis detection kit, and cell counting kit-8 (CCK8) assay kit were brought from Beyotime Biotechnology (Shanghai, China). GelMA was bought from Suzhou Yongqinquan Intelligent Equipment Co., Ltd (Suzhou, China), and the methacrylamide modification degree is 90 ± 5%.

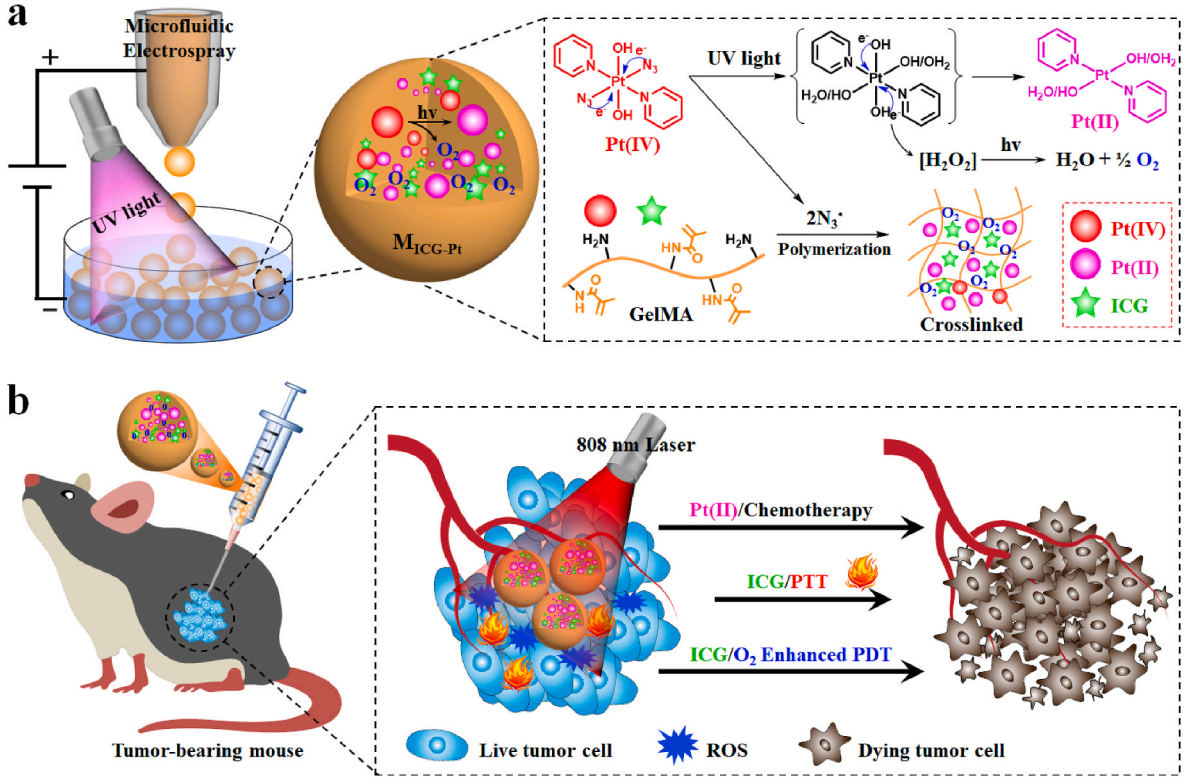

Fig. 1. Schematic illustration of the Pt(IV) prodrug initiated photo-polymerized microparticles ($M_{ICG\text{-}Pt}$) from microfluidic electrospray for synergistic tumor chemo-, photothermal and photodynamic therapy. (a) During the photo-activation of Pt(IV) to high cytotoxic Pt(II) species for chemotherapy, $N_3^{\bullet}$ and oxygen could also simultaneously generated. The $N_3^{\bullet}$ could induce the polymerization of GelMA matrix, ensuring the successful encapsulation of Pt(II) and ICG into the GelMA microparticles during microfluidic electrospray. Meanwhile, the oxygen could enhance the PDT efficacy of ICG. (b) After injection into the tumor site, the $M_{ICG\text{-}Pt}$ could efficiently eradicate the cancer cells for inhibiting the tumor growth *via* synergistic chemotherapy, PTT and PDT.

2.2. Synthesis of trans, trans,trans-[Pt(N$_3$)$_2$(OH)$_2$(py)$_2$] (Pt(IV))

Briefly, K_2PtCl_4 (2 g, 4.82 mmol) and pyridine (7.5 mL, 96.5 mmol) were dissolved into 50 mL of water, followed by heating to 75 °C for 90 min. Then, the solution was cooled to room temperature, filtered, and evaporated to produce white salt. Thereafter, 50 mL of HCl (2 M) solution was added, and the mixture was then heated for two days at 75 °C to produce a yellow suspension. The reaction solution was cooled, filtered, and then washed with cold minimum solvents (H_2O, ethanol, and ether) to produce the light yellow *trans*-[$PtCl_2(py)_2$ product. 1.1 g of *trans*-[$PtCl_2(py)_2$] (2.6 mmol) was dissolved in 100 mL water, before adding 954 mg of $AgNO_3$ (5.2 mmol) and stirring for 24 h. Then, the solution was filtered and added with NaN_3 (857 mg, 26 mmol). The reaction solution was stirred for 6 h to produce a yellow precipitate. *Trans*-[$Pt(N_3)_2(py)_2$] was produced after the solution was filtered out and the crude product was successively washed with minimum H_2O, ethanol, and ether. *Trans*-[$PtCl_2(py)_2$]: ^{1}H nuclear magnetic resonance (NMR) spectroscopy: δ = 8.79 ppm (a, NCH), 7.53 ppm (b, CH), 8.02 ppm (c, CH). *Trans*-[$Pt(N_3)_2(py)_2$]: ^{1}H NMR: δ = 8.63 ppm (a, NCH), 7.70 ppm (b, CH), 8.17 ppm (c, CH). The *trans*-[$Pt(N_3)_2(py)_2$] was oxidized by H_2O_2 (30%) for 4 h to get the final product of Pt(IV). Pt(IV): ^{1}H NMR: δ = 9.10 ppm (a, NCH), 7.85 ppm (b, CH), 8.26 ppm (c, CH). ^{13}C NMR: δ = 149.31 ppm (a, NCH), 126.48 ppm (b, CH), 142.19 ppm (c, CH). ESI-MS (MeOH), *m/z*, M = Pt(IV): $[M + Na]^+$ 494.1, $[(M)_2 + Na]^+$. 965.0.

2.3. Photo-degradation of Pt(IV)

Before recording the changes of absorbances of Pt(IV) *via* UV–vis–NIR spectrometer (Agilent, CARY5000, USA), the solution containing 20 μg mL^{-1} of Pt(IV) was irradiated by UV light for different time intervals. The valence state of Pt elements before and after irradiation was detected by X-ray photoelectron spectroscopy (XPS, Thermo ESCALAB 250). Power intensity of UV light: 365 nm, 1.25 W cm^{-2}.

2.4. Azidyl radical ($N_3^{\bullet}$) generation from Pt(IV)

Briefly, to a D_2O solution containing Pt(IV) (10 mM), DMPO (20 mM) along with or without Trp (2 mM) was added. Then, one of the solutions was irradiated by UV light for 1 min and the others were maintained in the dark. Subsequently, the solutions were detected by ^{1}H NMR spectroscopy (Bruker AVANCE DRX 400, Germany).

2.5. Pt(IV)-initiated photo-polymerization of GelMA hydrogel

For the preparation of GelMA hydrogel, a GelMA solution (30%, w/v) containing Pt(IV) (0.1% w/v) was firstly added in a vial, followed by UV light irradiating for 2 min. The photographs of the solution before and after gelation were taken by a camera. The storage modulus (G′) and loss modulus (G″) of GelMA hydrogel were investigated. In addition, the Pt(IV) initiated the polymerization of methacrylate alginate (AlgMA, 2.5%, w/v), polyethylene glycol diacrylate (PEGDA, 20%, w/v), and methacrylate silk fibroin (SilMA, 10%, w/v) was also investigated using the same method.

2.6. Preparation of the Pt(IV)-initiated photo-polymerization hydrogel microparticles from microfluidic electrospray

For the preparation of microfluidic electrospray hydrogel microparticles, a pregel solution containing Pt(IV) (2 mg mL^{-1}), ICG (100 μg mL^{-1}), and GelMA (30%) was firstly prepared. Then, the solution was transferred to a capillary microfluidic device using a cylindrical glass capillary tube with an orifice diameter of 300 μm. Finally, the pregel solution was pumped into the collection oil solution under electric force together with gravity. The flow rate of the syringe pump was set at 2 mL h^{-1}, and the voltage of the high-voltage power supply was set at 4 kV. During the preparation process, the ICG and Pt-drug-loaded microparticles were exposed to UV light for 2 min for gelatinization, and then the microparticles were washed with *n*-hexane three times before collection in a tube containing PBS for further use. Other microparticles with either ICG or Pt-drug loading were prepared as a control. To detect the drug loading capacity of microparticles, the microparticles were treated with collagenase solution for 7 days. Then, the Pt-drug and ICG release from the microparticles were measured by inductively coupled plasma optical emission spectrometry (ICP-OES) and UV–vis–NIR spectrometer, respectively.

2.7. Characterizations

A stereomicroscope (Olympus BX51, Tokyo, Japan) was applied to image the optical photographs of the microparticles. A field emission scanning electron microscope (SEM, SU8010, Hitachi, Japan) was used to observe the surface morphology and structure of the microparticles. Before imaging by SEM, the microparticles were firstly gradient dehydrated by 70%, 80%, 90%, and 100% ethanol, and then dried by supercritical drying.

2.8. Drug release in vitro

The microparticles (M_{Pt} or $M_{ICG\text{-}Pt}$) were placed into 10 mL PBS and incubated in an oscillating incubator for 192 h. At predetermined intervals throughout this procedure, 1 mL of the release medium was taken out and replaced with PBS solution in the same amount. The Pt contents of the collected medium were detected by inductively coupled plasma mass spectrometry (ICP-MS).

2.9. Photothermal effects

A series of ICG solutions with different concentrations were irradiated with 808-nm (0.6 W cm^{-2}) for 180 s. Then, the temperature elevations of the solutions were measured by an infrared thermal imager (FLIR E5-XT). Similarly, the microparticles (200 mg) with or without ICG loading were irradiated, and the temperature changes were measured in 180 s. Furthermore, the $M_{ICG\text{-}Pt}$ received 808-nm laser irradiation at various power intensities (0.3, 0.6, and 1.0 W cm^{-2}) was also investigated. Pure deionized water was irradiated as a control under the same condition. To detect the photothermal stability, the $M_{ICG\text{-}Pt}$ (200 mg) and free ICG (88.5 μg mL^{-1}) were irradiated by NIR light (0.6 W cm^{-2}) for 3 min (laser On), then naturally cooled for 3 min (laser Off). This On/Off cycle of NIR irradiation was repeated 5 times.

2.10. Detection of oxygen

The oxygen generated from Pt(IV) was detected by using [Ru(dpp)$_3$]Cl_2 (an oxygen probe) under UV light irradiation. The solution containing Pt(IV) (200 or 500 μg mL^{-1}) and [Ru(dpp)$_3$]Cl_2 (5 μM) was irradiated by UV light for different time intervals. Then, the fluorescence spectra from 500 to 800 nm of [Ru(dpp)$_3$]Cl_2 were recorded under a fluorescence spectrophotometer (Excitation wavelength: 470 nm). Power intensity of UV light: 365 nm, 1.25 W cm^{-2}.

To detect the oxygen stored in the microspheres, the $M_{ICG\text{-}Pt}$ (1.0 g) was dispersed in 5 mL of water containing collagenase at days 0, 1, 3, 5, and 7. After the degradation of the microparticles, the released oxygen dissolved in water was recorded by using an oxygen detection microsensor.

2.11. ROS generation

DPBF was employed to detect ROS generation from ICG. The solution containing Pt(IV) (10 μg mL^{-1}), ICG (10 μg mL^{-1}), and DPBF (15 μg mL^{-1}) received 808-nm laser irradiation for indicated time intervals. Then, the absorption spectra of DPBF were measured. To evaluate the

ROS generation increased by oxygen, the Pt(IV) was firstly irradiated by UV light (365 nm, 1.25 W cm^{-2}) to generate oxygen molecules, then the ICG and DPBF were added, and the solution was irradiated by the 808-nm laser before detection under the UV–vis–NIR spectrometer.

2.12. Intracellular ROS detection

A 24-well plate with 5×10^4 B16F10 cells per well was seeded, and cell attachment was then allowed to overnight. Following that, different microparticles were added to the cells and cultured for a further 12 h. Following the removal of the microparticles, M_{ICG} or $M_{ICG\text{-}Pt}$ treatment groups received 5 min of 808-nm laser irradiation. After that, the medium was taken out and replaced with new media containing DCFH-DA (10 M) for 30 min, before imaging by fluorescence microscopy.

2.13. In vitro antitumor effects

A 24-well plate with 5×10^4 B16F10 cells per well was seeded, and cell attachment was then allowed to overnight. Various microparticles were added and cultured for 12 h (Pt-content was 30 μg in M_{Pt} or $M_{ICG\text{-}Pt}$ treatment group). Then, M_{ICG} or $M_{ICG\text{-}Pt}$ treatment group was partially irradiated by the NIR laser for 5 min, followed by incubating for another 12 h. Other control groups were incubated for 24 h and maintained in dark. Thereafter, using live/dead staining, CCK8, and annexin V-FITC/PI apoptosis assays, the cytotoxicity of microparticles against cancer cells was investigated. Calcein-AM and PI were treated with the cells for live/dead staining, which was then viewed under a fluorescence microscope. For the CCK8 experiment, the cells were treated with the CCK8 reagent for 2 h, followed by measuring the absorbance at 450 nm using a microplate reader. For apoptosis evaluation, the cells were co-stained with Annexin V-FITC and PI and assessed for apoptosis by flow cytometry.

2.14. In vivo anti-tumor evaluation

After subcutaneously injecting 1×10^6 B16F10 cells into the mouse's right flank, the tumors were allowed to grow until their volume was close to 100 mm^3. Then, to detect the photothermal performance of the microparticles *in vivo*, the tumor sites were intratumor injected with PBS, M_B, M_{Pt}, M_{ICG}, and $M_{ICG\text{-}Pt}$, followed by irradiating with 808-nm laser for 5 min and monitoring temperature changes by an infrared thermal imager. Subsequently, the mice were randomized into seven groups (n = 3) at random: PBS (without irradiation, −), M_B (without irradiation, −), M_{Pt} (without irradiation, −), M_{ICG} (without irradiation, −), $M_{ICG\text{-}Pt}$ (without irradiation, −), M_{ICG} (with irradiation, +), and $M_{ICG\text{-}Pt}$ (with irradiation, +). The injection dose of Pt was 3.00 mg per kg body weight. Every two days, the mice's body weights and tumor volumes were noted. The mice were euthanized after 14 days. The primary organs and tumors were collected, fixed in 4% (v/v) paraformaldehyde, and sectioned into 5 m-thick sections for H&E and terminal-deoxynucleoitidyl transferase-mediated nick end labeling (TUNEL) staining. In addition, immunofluorescence staining HIF-1α was performed to observe hypoxia conditions in the tumor tissues. Power intensity of 808-nm laser: 0.6 W cm^{-2}, 10 min.

To further evaluate the anti-tumor efficacy of the prepared microparticles, 4T1 cells (1×10^6 cells per mouse) were subcutaneously injected into the right mammary of the mice, and then the tumor volumes were allowed to grow to approximately 100 mm^3. Before the anti-tumor experiments, the *in vivo* photothermal performance was also investigated. After the intratumor injection of different microparticles, the tumor sites were irradiated by 808-nm laser for 5 min and the temperature changes of the mice were observed by the infrared thermal imager. Subsequently, the mice have randomly divided into seven groups and each group has 6 mice (n = 6): PBS (without irradiation, −), M_B (without irradiation, −), M_{Pt} (without irradiation, −), M_{ICG} (without irradiation, −), $M_{ICG\text{-}Pt}$ (without irradiation, −), M_{ICG} (with irradiation, +), and $M_{ICG\text{-}Pt}$ (with irradiation, +). The injection dose of Pt was 3.00 mg per kg body weight. The tumor volumes and body weights of the mice were measured every other day. The tumor volumes were recorded as the following equation: length × $width^2$ × 0.5. At the end of the experiments, the tumors were collected for H&E and TUNEL staining.

All experimental designs and protocols involving animals were approved by the Animal Ethics Committee of the Wenzhou Institute, University of Chinese Academy of Sciences (approval WIUCAS21031002) and complied with the recommendations of the academy's animal research guidelines.

2.15. Biodistribution of Pt

When the tumor sizes reached ~100 mm^3, 4T1-tumor-bearing mice were intratumor injected with $M_{ICG\text{-}Pt}$ (n = 3). The injection dose of Pt was 3.00 mg per kg body weight. Tumors and major organs were collected and weighed at predetermined intervals. Then, the samples were treated with concentrated nitric acid to produce a transparent solution before the Pt content was determined by ICP-MS.

2.16. Statistical analysis

Unless otherwise specified, the other experiments had triple replicates (n = 3). All statistical data are expressed as the mean ± SD. Statistical significance was calculated *via* unpaired Student's t-tests. *$p < 0.05$, **$p < 0.01$, ***$p < 0.001$.

3. Results and discussion

3.1. Synthesis and characterization of Pt(IV)

To start with, we synthesized the Pt(IV) prodrug step by step according to the procedures in Fig. S1a. The intermediate product of *trans*-$[PtCl_2(py)_2]$ and *trans*-$[Pt(N_3)(py)_2]$ could be measured by ^{1}H NMR spectroscopy, and the successful synthesis of Pt(IV) was also verified by ^{1}H NMR, ^{13}C NMR spectroscopy and electrospray ionization mass spectrometry (ESI-MS) (Fig. 2a,b and S1,S2). Considering the photosensitivity of the Pt(IV)−azide prodrugs, the photodegradation behavior of the synthesized Pt(IV) was investigated *via* a UV–vis–NIR spectrophotometer. As observed in Fig. 2c, the absorbance of Pt(IV) under UV light irradiation significantly reduced with the extension of the irradiation time. The photodegradation process was in accord with the first-order kinetics by calculating the degradation rate of the absorption value at 289 nm (Fig. 2d). Besides, the results of the X-ray photoelectron spectroscopy (XPS) measurement indicated that following irradiation, the Pt(IV) (Pt_{4f} at 78.8 eV and 75.4 eV) was reduced to Pt(II) species (Pt_{4f} at 75.9 eV and 72.7 eV) with evidently changed binding energies (Fig. 2e). The possible degradation process of Pt(IV) could be described in Fig. S3. In addition to the Pt(II) generation, the $N_3^{\bullet}$ could also be effectively generated from Pt(IV) during the photoreduction process. To verify this, dimethyl pyridine *N*-oxide (DMPO) was employed as a radical trap, and the mixed solution of Pt(IV) and DMPO after irradiation for 1 min by UV light was measured through ^{1}H NMR spectroscopy (Fig. 2f). It could be found that the characteristic peaks of Pt(IV) (denoted by shuriken) were gradually reduced, and the peaks of DMPO capturing $N_3^{\bullet}$ (DMPO-N_3, denoted by circle) were shown with relatively high intensities. Evidently, the addition of tryptophan (Trp) as an $N_3^{\bullet}$ quencher could significantly inhibit the binding reaction between DMPO and $N_3^{\bullet}$. The characteristic peaks of DMPO-N_3 were obviously decreased in the ^{1}H NMR spectra, further confirming the efficient generation of $N_3^{\bullet}$ from Pt(IV). Furthermore, the oxygen generation capacity of Pt(IV) after irradiation was detected by $[Ru(dpp)_3]Cl_2$ (an oxygen detection probe), whose fluorescence would be sensitively dampened by oxygen molecules. The fluorescence intensity of $[Ru(dpp)_3]Cl_2$ incubated with Pt(IV) was obviously weakened after UV irradiation, and the declination process was accelerated with the increase of Pt(IV)

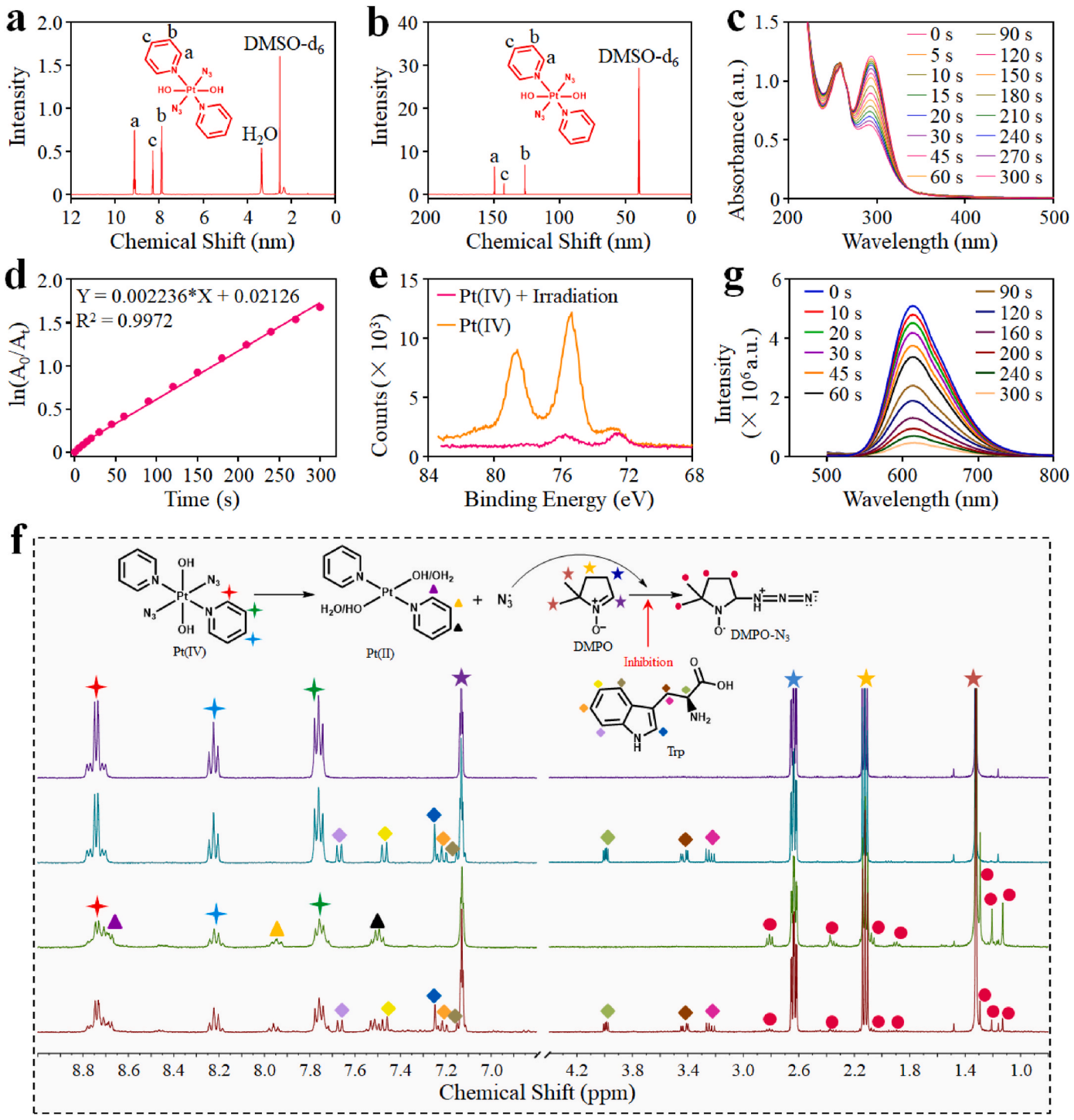

Fig. 2. Synthesis, photo-reduction, azidyl radical ($N_3^{\bullet}$), and O_2 generation of the Pt(IV) prodrug. (a, b) ^1H NMR (a) and ^{13}C NMR (b) specta of Pt(IV). (c) UV–vis spectra of Pt(IV) after UV irradiation for indicated time intervals. (d) The first-order kinetics of Pt(IV) degradation under UV irradiation. (e) XPS analysis of Pt(IV) before and after irradiation. (f) ^1H NMR spectra of Pt(IV) and DMPO in D_2O: (*i*, *iii*) without Trp, (*ii*, *iv*) with Trp; (*i*, *ii*) without irradiation, (*iii*, *iv*) irradiation for 60 s. Assignments: stars represent the peaks of DMPO; shuriken represent the peaks of Pt(IV); triangles represent the peaks of Pt(II); prismatic represent the peaks of Trp; circles represent the peaks of DMPO-$N_3^{\bullet}$ photoproducts. (g) Fluorescence spectra of $[Ru(dpp)_3]Cl_2$ incubated with Pt(IV) (200 μg mL^{-1}) under UV irradiation at different time intervals.

concentration (Fig. 2g and S4b). By contrast, it displayed negligible changes in the absence of Pt(IV) after light irradiation (Fig. S4c), demonstrating the oxygen generation during the photoactivation process of Pt(IV). Collectively, the above data demonstrated the successful synthesis of the Pt(IV), which could be degraded to Pt(II) species under UV irradiation, concurrently generating $N_3^{\bullet}$ and oxygen.

3.2. Preparation and characterization of hydrogel microparticles

Subsequently, the $N_3^{\bullet}$-induced photo-polymerization of the GelMA matrix was investigated. The Pt(IV) was added to the solution containing GelMA (Fig. S5) and then irradiated by UV light. As shown in Fig. 3a, the transformation process of the fluid solution to solid hydrogel could be

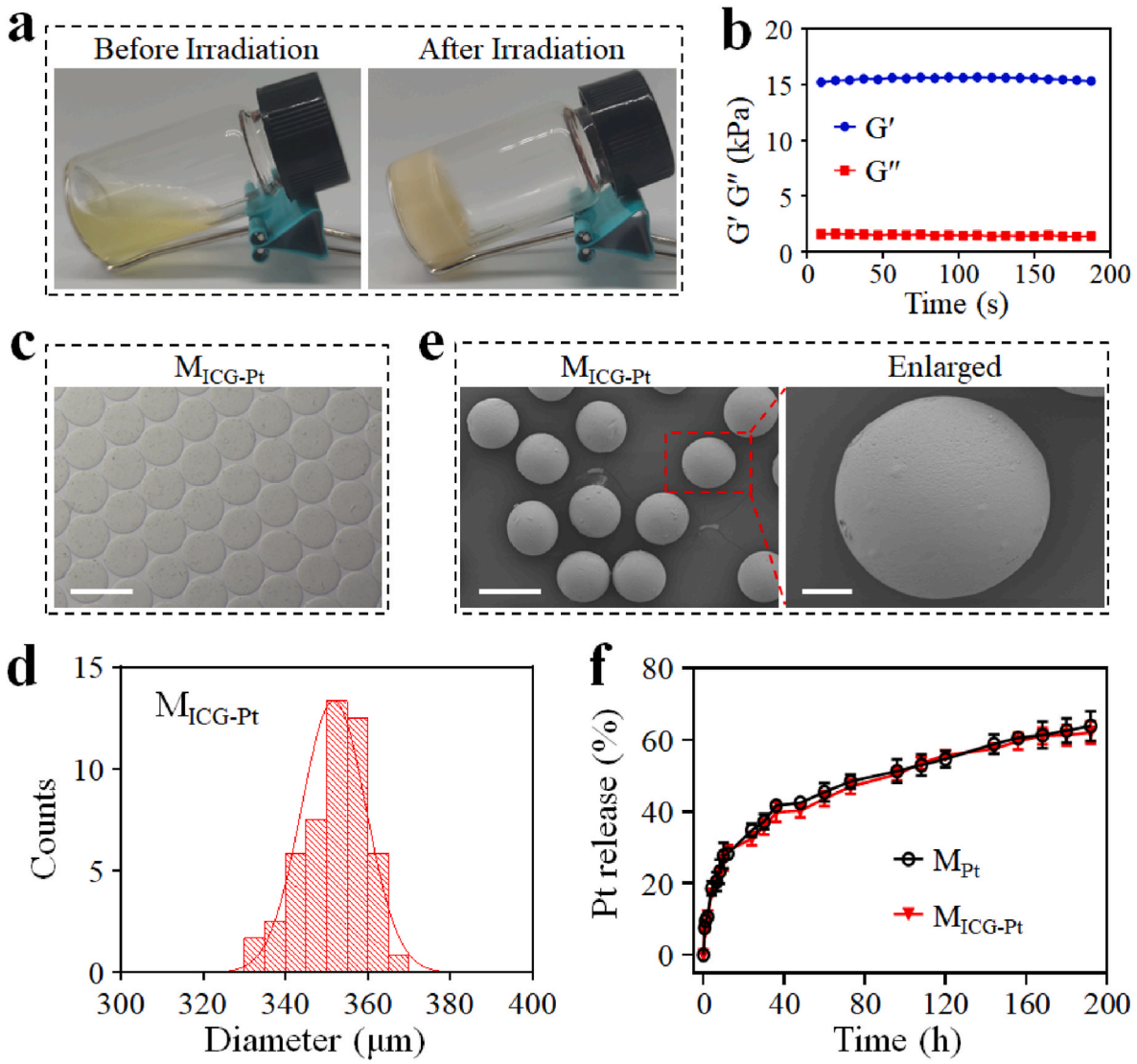

Fig. 3. Characterization of hydrogel microparticles. (a) Photographs of the GelMA solution and hydrogel before and after UV irradiation. (b) The storage modulus (G′) and loss modulus (G″) of GelMA hydrogel. (c, d) Optical image (c), and corresponding size distribution (d) of $M_{ICG\text{-}Pt}$ (Scale bar: 500 μm). (e) SEM images of $M_{ICG\text{-}Pt}$ (Scale bar, left: 250 μm; right: 50 μm). (f) The Pt release profiles of M_{Pt} and $M_{ICG\text{-}Pt}$.

clearly observed in a transparent vial after UV irradiation, indicating that the $N_3^{\bullet}$ generated from Pt(IV) could effectively trigger the photo-polymerization of GelMA. Besides, the storage modulus (G′) of GelMA hydrogel was much higher than the loss modulus (G″), further confirming the formation of true gels (Fig. 3b). To verify the universality of Pt(IV) prodrug as a photo-polymerization initiator, we used the Pt(IV) to initiate the polymerization of methacrylate alginate (AlgMA), polyethylene glycol diacrylate (PEGDA), and methacrylate silk fibroin (SilMA) solutions. Similar to the GelMA, it could be found that the formation of AlgMA, PEGDA, and SilMA hydrogels was clearly observed in the transparent vials, indicating the universality of Pt(IV) to initiate photo-polymerization of multiple matrixes (Fig. S6). Then, microfluidic electrospray technology was employed to prepare Pt-drug and ICG-loaded microparticles. The microfluidic chip was used as a microfluidic electrospray head to be integrated into a microfluidic electrospray system (Fig. S7). Then, the mixture of Pt(IV), GelMA, and ICG was pumped by a syringe pump to form droplets under the electric force together with gravity. After that, the droplets were gelatinized in the collection oil pool under UV light irradiation. The successful preparation of microparticles was verified by a camera, photon microscope, and scanning electron microscope (SEM) (Fig. 3c–e and S8-S10). As a control, the microparticles (M_B) without Pt-drug or ICG loading and the microparticles (M_{ICG}) with only ICG loading were gelatinized using lithium phenyl-2,4,6-trimethylbenzoylphosphinate (LAP, a typical photoinitiator). Because of their unique colors of Pt-drug and ICG, the M_{Pt}, and M_{ICG} respectively displayed yellow and green colors in the tubes, while the M_B without Pt-drug and ICG appeared in white and the $M_{ICG\text{-}Pt}$ presented both colors of Pt-drug and ICG (Fig. S8). All microparticles were spherical in shape as observed by optical microscope, and the average diameters of M_B, M_{Pt}, M_{ICG} and $M_{ICG\text{-}Pt}$ were 347.0 ± 8.0 μm, 341.6 ± 8.8 μm, 346.3 ± 10.0 μm, and 351.7 ± 7.8 μm, respectively (Fig. 3c,d and S9). Before observation under SEM, the hydrogel microparticles were orderly dehydrated in a series of different concentrations of ethanol and then dried using a supercritical drying method. Thus, the spherical morphologies of the microparticles were maintained. But the average diameter of microparticles significantly decreased to less than 300 μm after the dehydration (Fig. 3e and S10). The Pt-drug and ICG contents of $M_{ICG\text{-}Pt}$ detected by ICP-OES and UV–vis–NIR spectrometer were determined to be 1.8 mg g^{-1} and 88.5 μg g^{-1}, respectively. Subsequently, the Pt-drug release behaviors of M_{Pt} and $M_{ICG\text{-}Pt}$ were investigated, and their profiles indicated that the M_{Pt} and $M_{ICG\text{-}Pt}$ displayed similar drug release behavior. Quantificationally, 35% and 32% of Pt

were released from M_{Pt} and M_{ICG-Pt} within 24 h, and the cumulative release amounts finally reached 64% and 62% in 192 h, respectively (Fig. 3f). Taken together, these results indicated the successful preparation of Pt-drug and ICG loading microparticles, which maintained a sustained drug release behavior *in vitro*.

3.3. Photothermal and photodynamic effects of hydrogel microparticles

As a well-known organic dye approved by Food and Drug Administration (FDA), ICG has been widely used for PTT and PDT. As verified by the photothermal heating curves, ICG can absorb NIR light and convert it to heat energy (Fig. S11). The temperature of the ICG solution gradually increased with the extension time of 808-nm laser irradiation, which was exacerbated with the increase of ICG concentrations. Similarly, the ICG-loaded microparticles of M_{ICG} and M_{ICG-Pt} also displayed photothermal heating effects under NIR light irradiation (Fig. 4a). A considerable temperature elevation was observed for both M_{ICG} (Δ34.0 °C) and M_{ICG-Pt} (Δ34.3 °C) under NIR light irradiation for 3 min, in contrast to the negligible temperature increase for the microparticles without loading ICG (Δ2.0 °C) under the same condition. The thermal photographs could directly reveal the above NIR-induced photothermal heating process of M_{ICG-Pt} (Fig. S12). Besides, the photothermal temperature of M_{ICG-Pt} was evidently increased with the increase of laser power density (Fig. 4b). Furthermore, compared with the noticeable change in the photothermal effect of ICG solution under repetitive five NIR-On/Off cycles, little temperature deterioration happened on M_{ICG-Pt} under the same conditions (Fig. 4c). Because of the saturated double bonds on the conjugated chain, ICG molecules will be degraded and photobleached under NIR light irradiation, resulting in the decrease of NIR absorption capacity and photothermal conversion efficiency [47, 48]. In comparison, by evenly dispersing ICG molecules inside the microparticles, the hydrophobic interactions between free ICG might be

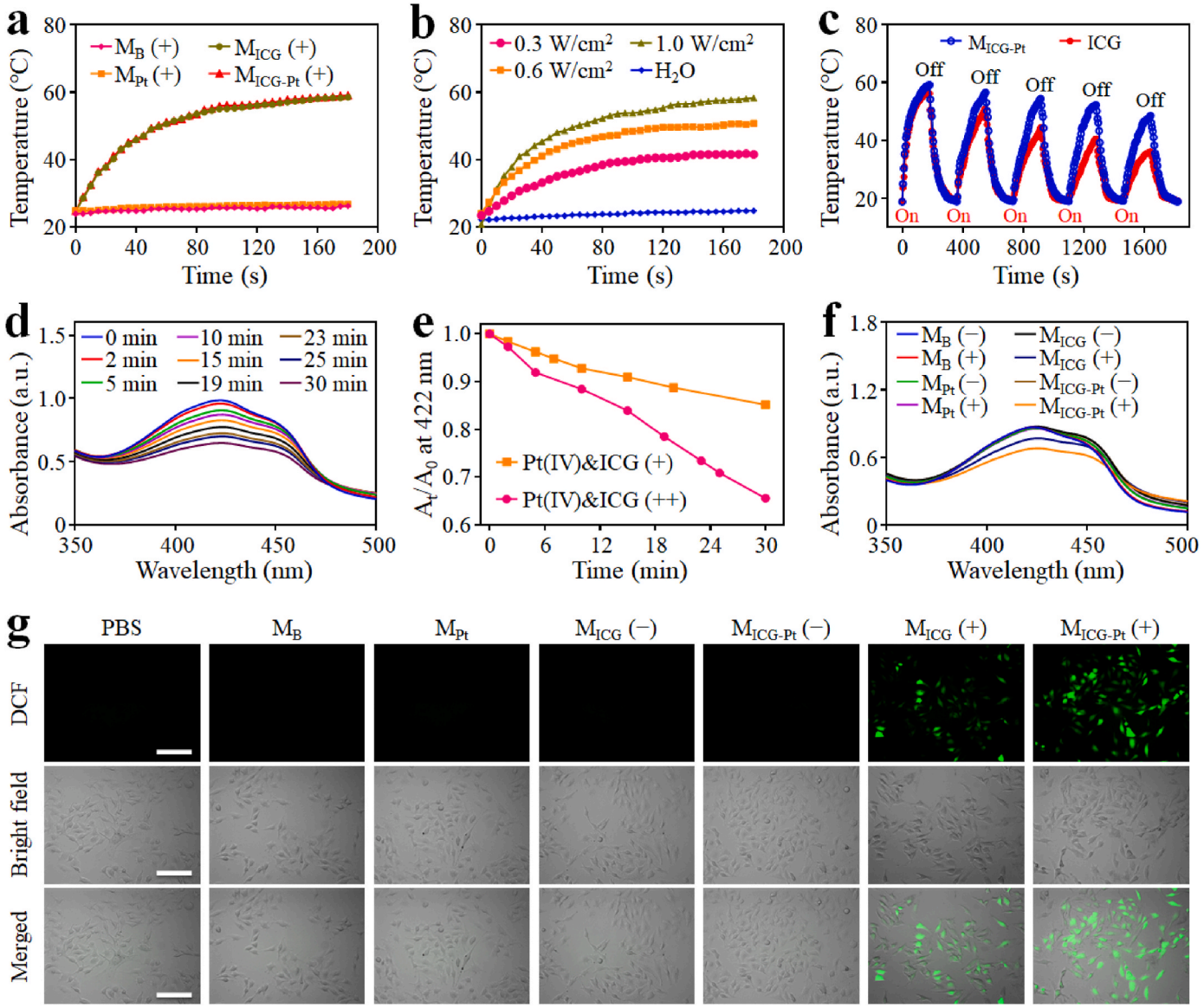

Fig. 4. *In vitro* simultaneous PTT/PDT effects of M_{ICG-Pt}. (a) Photothermal heating curves of different microparticles under 808-nm laser irradiation (0.6 W cm^{-2}). (b) Photothermal heating curves of M_{ICG-Pt} with different laser power densities. (c) Temperature variation of M_{ICG-Pt} and ICG over five NIR-On/Off cycles (808-nm, 0.6 W cm^{-2}, On or Off for 3 min). (d) Time-dependent UV absorption spectra of DPBF incubated with Pt(IV)&ICG (++) under 808-nm irradiation from 0 to 30 min (++) indicated that the Pt(IV) was firstly irradiation by UV light before adding ICG and then irradiated by NIR laser. (e) Comparison of the decay rate of DPBF at 422 nm after incubation with Pt(IV)&ICG (+) or Pt(IV)&ICG (++) solution under the 808-nm irradiation. (+) indicated that the Pt(IV) was not irradiation by UV light before adding ICG. (f) Time-dependent UV absorption spectra of DPBF incubated with different microparticles with or without 808-nm laser irradiation for 30 min. (g) Intracellular ROS detection by incubating DCFH-DA with different microparticles under the 808-nm laser irradiation at 0.6 W cm^{-2} for 5 min.

reduced, which would reduce the aggregation and protect the chemical structure for improving the stability of ICG molecules. Therefore, the photostability of ICG would be reasonably improved after being loaded in the microparticles. All the above results indicated the good photothermal performance of the ICG-loaded microparticles, which could greatly facilitate the further photothermal ablation of tumors.

To further validate the photodynamic effects of the ICG, 1,3-diphenylisobenzofuran (DPBF, an indicator) was employed to detect ROS generation. It was found that the absorbance at 422 nm of DPBF solution containing Pt(IV) and ICG continuously decreased after NIR irradiation, while the absorbance of pure DPBF solution displayed a minimal change under the same irradiation condition (Fig. S13). As a contrast, before the addition of ICG and DPBF, the Pt(IV) solution was firstly irradiated by UV light for 1 min, and then the mixed solution was exposed to the NIR irradiation. A much higher decrease rate of DPBF absorbance could be monitored, which is proper because the O_2 generated from Pt(IV) after UV light irradiation and thereby promote the ROS generation from ICG (Fig. 4d and e). Similarly, under the irradiation of NIR laser, the microparticles loading ICG could significantly influence the absorbance of DPBF, and the decay rate induced by M_{ICG-Pt} is evidently higher than that of M_{ICG}, which could be attributed to the generation storage of O_2 molecules in the M_{ICG-Pt} during the preparation process (Fig. 4f and S14). Furthermore, the ROS generation in living cells was verified using the 2′,7-dichlorodihydrofluorescein diacetate (DCFH-DA) as an indicator because it could be oxidized by ROS to fluorescent dichlorofluorescein (DCF). As shown in Fig. 4g, a bright green fluorescence of DCF appeared in M_{ICG} and M_{ICG-Pt} treated cells under NIR irradiation, indicating the ROS generation in living cells. On the contrary, negligible

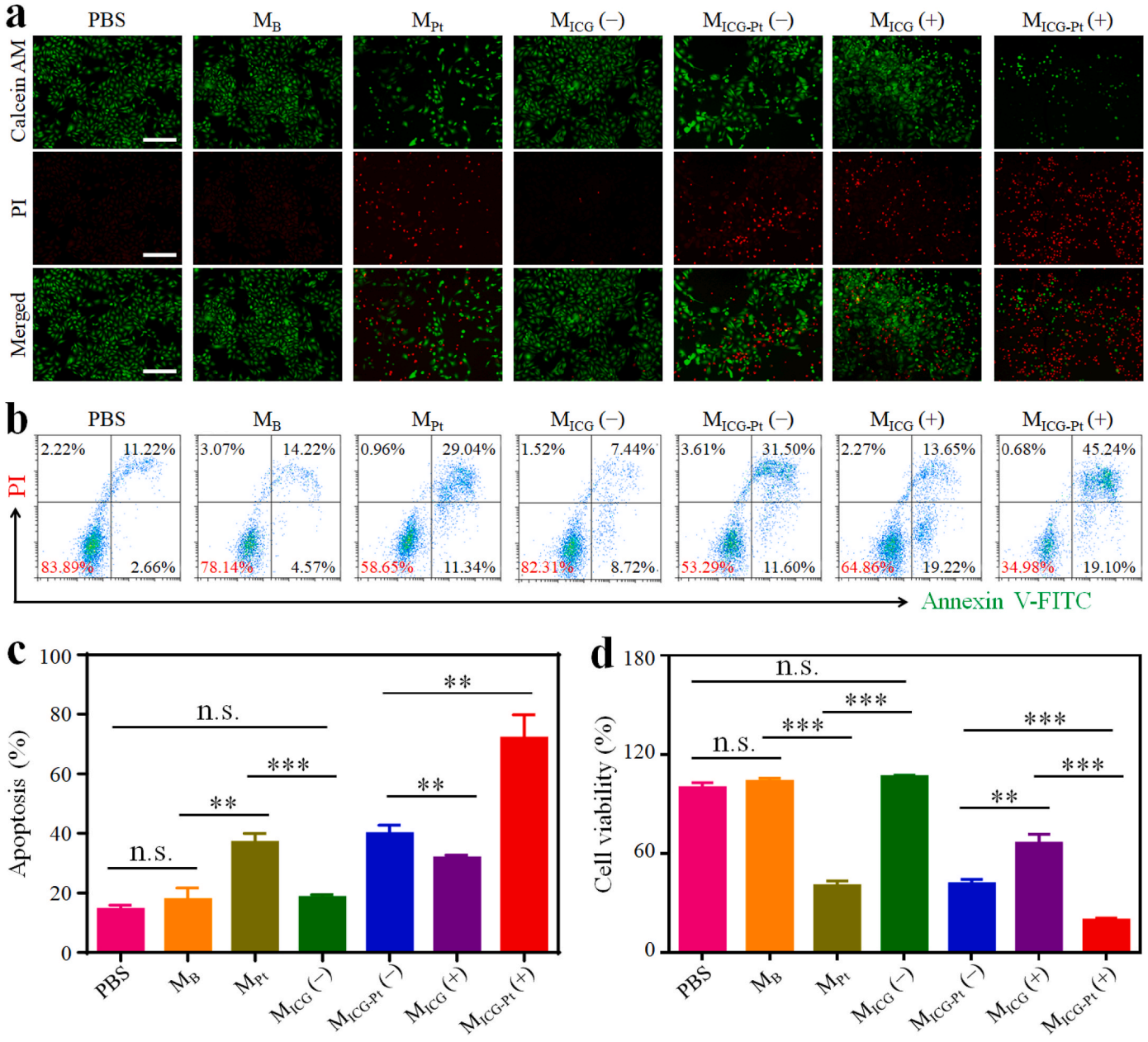

Fig. 5. *In vitro* antitumor efficacy of M_{ICG-Pt}. (a) Live/dead staining of B16F10 cells after incubation with different microparticles for 24 h. Scale bar, 100 μm. (b, c) Apoptosis analysis (b) by flow cytometry and corresponding apoptosis rates (c) of B16F10 cells after incubation with different microparticles for 24 h. (d) CCK8 assay of B16F10 cells after incubation with different microparticles for 24 h (−) indicated without NIR irradiation, and (+) indicated with NIR irradiation (808-nm, 0.6 W cm^{-2}, 5 min). All the cell experiments had three independent replicates (n = 3). Data are presented as the mean ± SD. n.s.: no significance, *p < 0.05, **p < 0.01, ***p < 0.001.

green fluorescence was seen in the other groups with or without NIR irradiation. These results indicated the satisfactory photodynamic effects of M_{ICG-Pt} under NIR irradiation.

3.4. In vitro antitumor efficacy

To further evaluate the *in vitro* antitumor efficacy of the prepared composite microparticles, the live/dead detection by calcein-AM/propidium iodide (PI) staining, apoptosis analysis by flow cytometry, and cell viability by CCK8 assay were conducted by incubating different microparticles with mouse melanoma B16F10 cells. Live/dead assay showed that a large number of cells were dead after the treatment with M_{Pt} and M_{ICG-Pt} even without NIR irradiation, indicating the strong chemotherapeutic efficacy of Pt-drug-laden microparticles (Fig. 5a). By contrast, the treatments of M_B and M_{ICG} without Pt-drug loading displayed no cytotoxicity against B16F10 cells, implying the good biocompatibility of the pure microparticles and ICG molecules. However, when exposed to NIR irradiation, a considerable number of cells were dead when incubated with M_{ICG}, confirming the phototherapeutic effects of ICG. Furthermore, almost all cells were dead when incubated with M_{ICG-Pt} under NIR irradiation, indicating the excellent antitumor effect of synergetic chemotherapy, PTT, and PDT. The flow cytometry results showed that the apoptosis rates of M_{Pt} and M_{ICG-Pt} treated cells without irradiation were 36.95% and 39.91%, respectively, and the M_{ICG} treatment group with irradiation displayed an apoptosis rate of 31.76%. As expected, the M_{ICG-Pt} with NIR irradiation had the best killing effect against cancer cells with an apoptosis rate of 71.96% (Fig. 5b and c). Consistently, CCK8 results also demonstrated the significant tumor therapeutic efficacy of M_{ICG-Pt} with NIR irradiation (Fig. 5d). All results above indicated that the M_{ICG-Pt} could effectively kill tumor cells *via* synergetic chemotherapy, PTT, and PDT under the NIR irradiation.

3.5. In vivo antitumor efficacy and mechanism

Having confirmed the efficient *in vitro* antitumor capacity of M_{ICG-Pt}, the *in vivo* tumor inhibition experiments were carried out using a subcutaneous B16F10 xenograft mouse model. Firstly, the *in vivo* photothermal effects were investigated by irradiating the tumors at 12 h after the intratumor injection of different microparticles. After receiving NIR radiation for 5 min, the temperature elevation on the tumor treated with PBS, M_B, and M_{Pt} was only approximately 4.5 °C, whereas the temperature in the M_{ICG} and M_{ICG-Pt} groups could reach about 54 °C (Fig. 6a and S15). After 14 days, the NIR-irradiated M_{ICG-Pt} group showed the best tumor inhibition efficacy with the lowest tumor volume of about 36 mm^3 and the lightest tumor weight of about 0.03 g among all groups (Fig. 6b–d). Besides, all mice's body weights increased steadily during the experiment, and no obvious pathologic abnormalities could be noticed in the major organs stained with H&E, demonstrating the minimal systemic toxicity of the microparticles (Fig. 6e and S16).

In order to investigate the synergistic anti-tumor mechanisms of M_{ICG-Pt}, H&E, TUNEL, and immunofluorescence staining on tumor slices were studied. H&E analysis showed that the treatments of M_{ICG} (+) resulted in significant necrosis of tumor cells, which was more obvious in the M_{ICG-Pt} (+) treated group (Fig. 7a). In contrast, the tumor cells were densely populated without obvious cellular nuclear shrinkage or disappearance in the control, M_B and M_{ICG} groups without irradiation. Quantitatively, the percentage of tumor cells in the M_{ICG-Pt} (+) group was 30.74%, evidently lower than that in PBS (98.41%), M_B (96.10%), M_{Pt} (50.42%), M_{ICG} (−, 96.73%), M_{ICG-Pt} (−, 44.11%), M_{ICG} (+, 60.76%) groups (Fig. 7b). The TUNEL staining revealed similar results that the M_{ICG-Pt} (+) group had the most apoptosis rate of 84.32%, significantly higher than other groups (Fig. 7a,c). In addition, the hypoxia conditions of tumors were evaluated by immunofluorescence staining of HIF-1α (an indicator of hypoxia). Owing to the O_2 generation from Pt(IV) during the

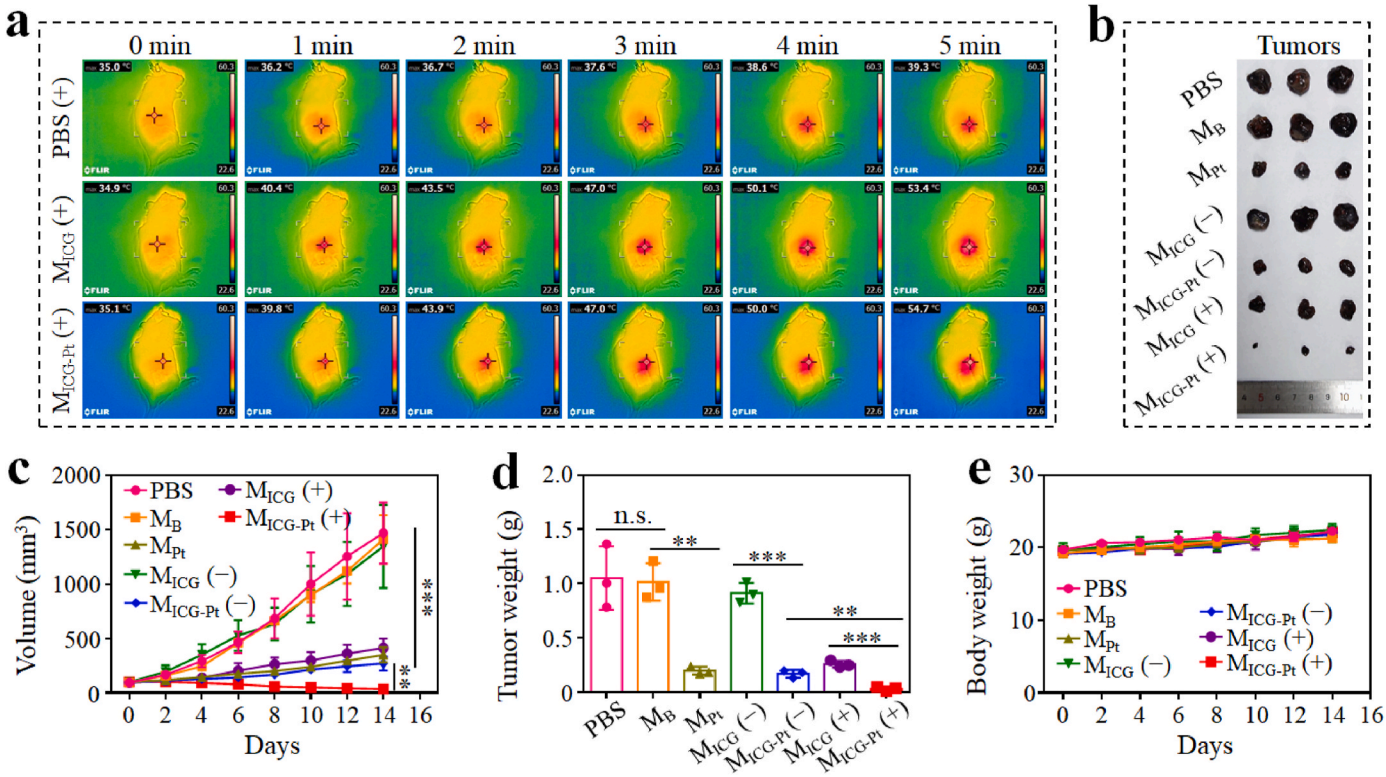

Fig. 6. *In vivo* synergistic chemotherapy, PTT, and PDT of M_{ICG-Pt} on B16F10 tumor model. (a) Infrared thermal images of B16F10 tumor-bearing mice intratumorally injected with PBS, M_{ICG} or M_{ICG-Pt} and irradiated by 808-nm laser (0.6 W cm^{-2}) for 5 min. (b–e) Tumor photographs (b), tumor volumes (c), tumor weights (d), and body weight (e) changes of mice after various treatments for 14 days. (−) indicated without NIR irradiation, and (+) indicated with NIR irradiation. Each experiment group has 3 mice (n = 3). Data are presented as the mean ± SD. n.s.: no significance, *p < 0.05, **p < 0.01, ***p < 0.001.

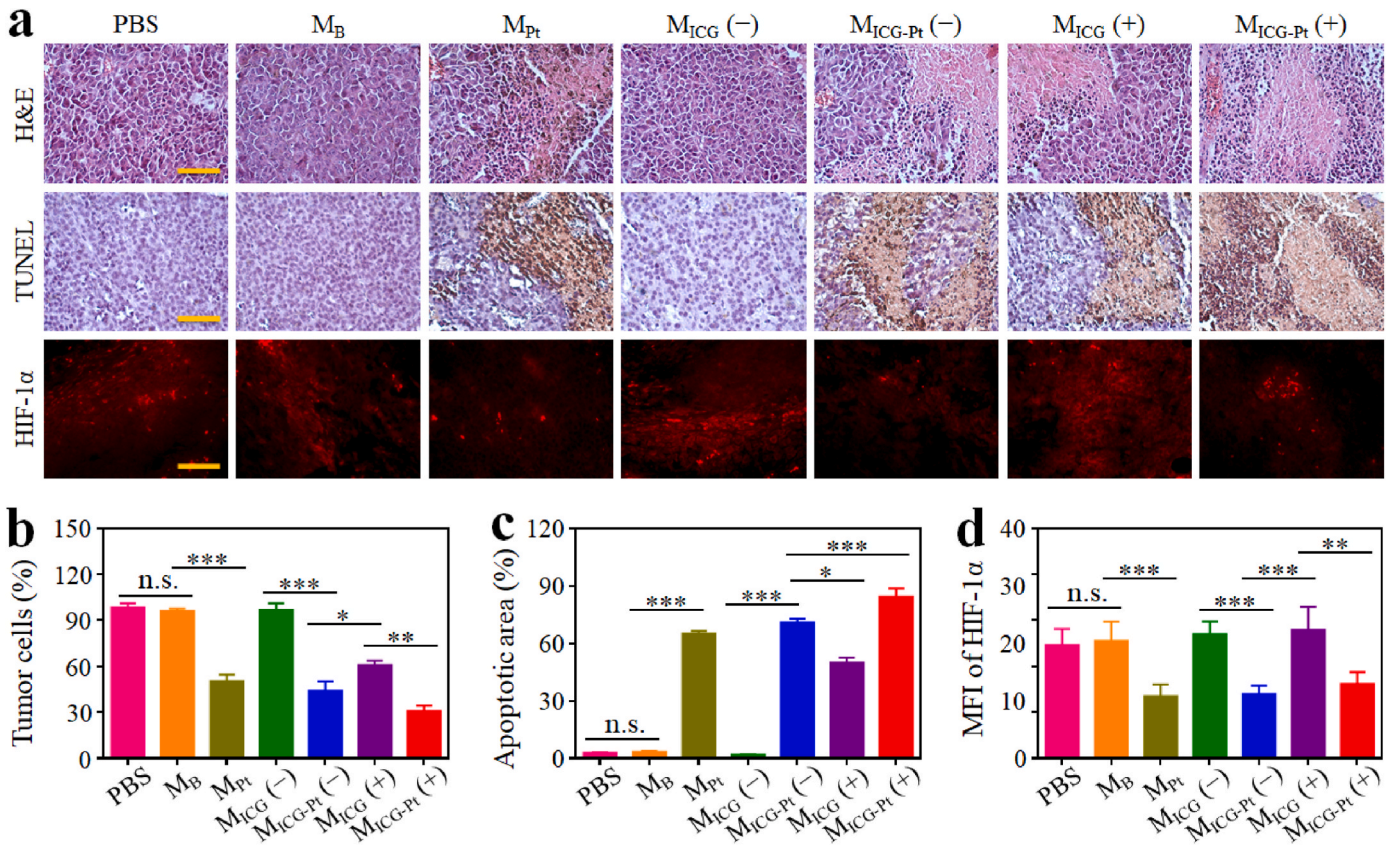

Fig. 7. Immunohistochemistry and immunofluorescence analyses. (a) H&E, TUNEL, and HIF-1α staining images of tumor tissues after various treatments. Scale bar, 50 μm. (b–d) Quantification of the H&E (b), TUNEL (c), and HIF-1α (d) staining assays. (−) indicated without NIR irradiation, and (+) indicated with NIR irradiation. Each experiment group has 3 mice (n = 3). Data are presented as the mean ± SD. n.s.: no significance, *$p < 0.05$, **$p < 0.01$, ***$p < 0.001$.

microfluidic electrospray process, plenty of O_2 molecules were encapsulated in the M_{Pt} and M_{ICG-Pt}, which could alleviate the hypoxia conditions in tumors. As shown in Fig. 7a, the red fluorescence of M_{Pt} and M_{ICG-Pt} injection groups was evidently decreased. The mean fluorescence intensities of M_{Pt} and M_{ICG-Pt} treatments without irradiation were 13.46 and 13.99, respectively, obviously lower than those of control, M_B, and M_{ICG} treatment groups with or without irradiation (Fig. 7d). During the PDT process, many O_2 molecules will be consumed. Therefore, compared with the M_{ICG} (+) group without loading O_2 molecules, the O_2 content in M_{ICG-Pt} (+) was higher. Thus, the mean fluorescence intensities of the M_{ICG-Pt} (+) treatment group were lower than that of the M_{ICG} (+) group (Fig. 7d). All these findings suggested that the M_{ICG-Pt} could effectively suppress tumor growth by alleviating tumor hypoxia and inducing necrosis/apoptosis of tumor cells *in vivo*.

To further evaluate whether our proposed microparticle-based multimodal therapy platform could be broadly applicable, we performed antitumor experiments on orthotopic breast cancer 4T1 tumor mouse mode. The administration processes were consistent with those of the B16F10 xenograft mouse model. Similarly, the *in vivo* photothermal effects of M_{ICG} and M_{ICG-Pt} injection groups could also be observed in the orthotopic breast cancer mouse mode. The temperature could be significantly elevated to 53.0 °C in M_{ICG} and M_{ICG-Pt} treatment groups under 808-nm irradiation for 5 min, in contrast to the only 4.1 °C increase for the control group (Fig. 8a). As observed during the experiments, the control, M_B and M_{ICG} (−) groups could hardly suppress the growth of the tumors (Fig. 8b–d). Due to the PDT and PTT effects, the M_{ICG} (+) administration could inhibit the growth of tumors to a certain degree. Because of the sustained release of Pt-drug after microparticle injection (Fig. S17), the M_{Pt} and M_{ICG-Pt} (−) groups could further control the tumor growth *via* the sustained chemotherapy action. Notably, the M_{ICG-Pt} (+) led to the maximal inhibition of tumors with the smallest tumor volume (~150 mm^3) and the lightest tumor weight (~0.12 g) due to the synergistic chemotherapy, PTT, and PDT. As expected, the M_{ICG-Pt} (+)-treated group induced the most severe histological damages and the strongest apoptosis effects in tumor tissues among all groups as observed in H&E and TUNEL staining, respectively (Fig. 8e). During the experiments, the body weights of each group were all increased, indicating the safety of the prepared microparticles (Fig. 8f). These results further demonstrated that the developed microparticles are efficient composite formulas for synergistic chemotherapy, PTT, and PDT with high safety and potent efficacy.

4. Conclusions

In summary, we have presented Pt(IV) prodrug-initiated photopolymerized hydrogel microparticles (M_{ICG-Pt}) by using droplet microfluidics for synergistic tumor chemo-, photothermal and photodynamic therapy. The Pt(IV) prodrug could be transformed to cytotoxic Pt(II) under UV irradiation for tumor chemotherapy, which simultaneously generated $N_3^{\bullet}$ for the polymerization of GelMA and oxygen for enhanced PDT, respectively. In addition, ICG was also encapsulated in the microcarriers for synergistic PTT/PDT upon NIR irradiation. Therefore, the obtained M_{ICG-Pt} could not only significantly kill cancer cells *in vitro*, but also substantially inhibited tumor growth *in vivo via* synergistic chemotherapy, PTT, and PDT. Our results indicated that such Pt(IV)-initiated hydrogel microparticles provided an effective and versatile therapeutic platform for various tumor treatments.

Ethics approval

All experimental designs and protocols involving animals were approved by the Animal Ethics Committee of the Wenzhou Institute,

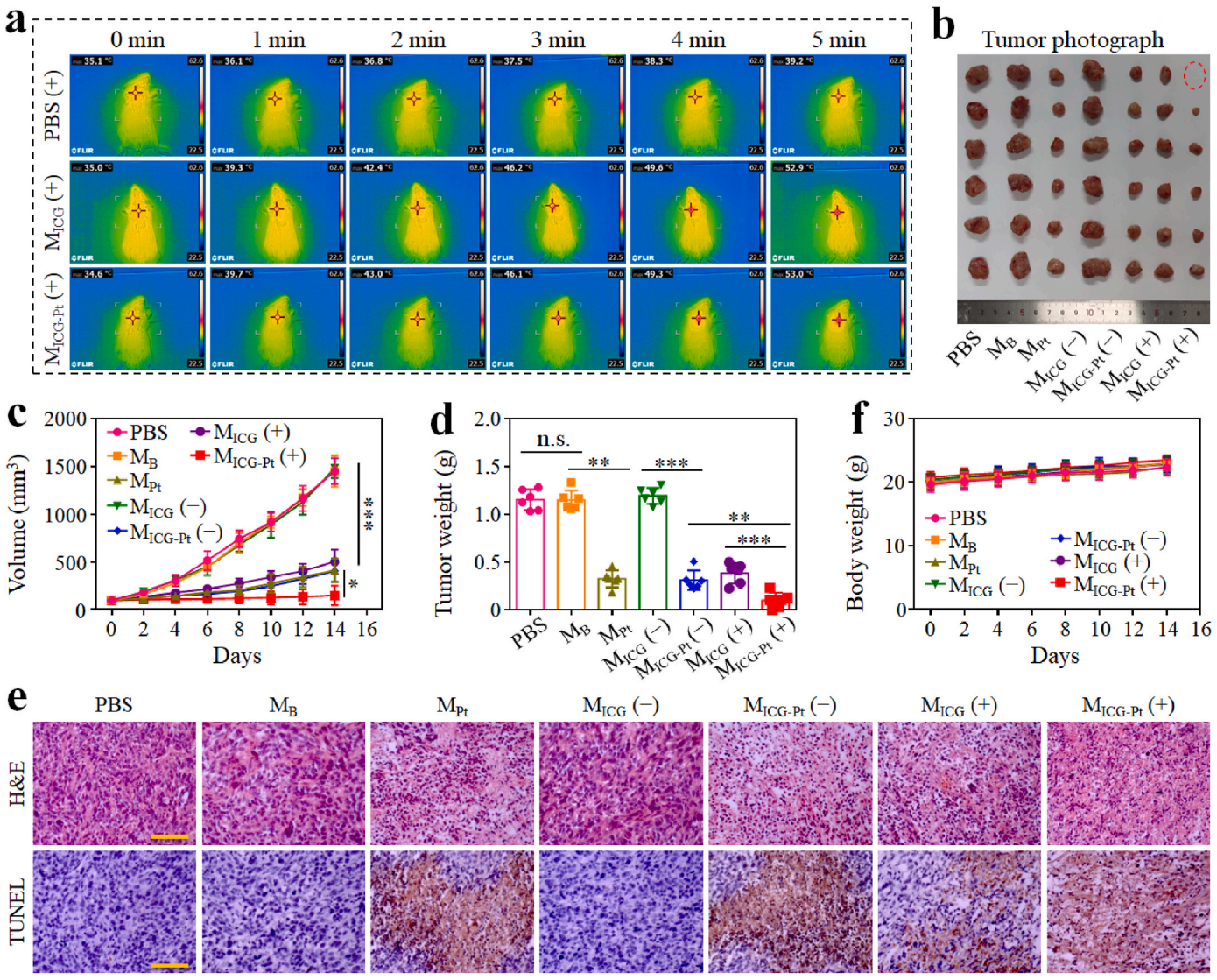

Fig. 8. *In vivo* synergistic chemotherapy, PTT, and PDT of M_{ICG-Pt} on 4T1 tumor model. (a) Infrared thermal images of 4T1 tumor-bearing mice intratumorally injected with PBS, M_{ICG} or M_{ICG-Pt} and irradiated by 808-nm laser (0.6 W cm^{-2}) for 5 min. (b–d) Tumor photographs (b), tumor volumes (c), and tumor weights (d) of mice after various treatments for 14 days. (e) H&E and TUNEL staining images of tumor tissues after various treatments. Scale bar, 50 μm. (f) Body weight changes of mice after various treatments for 14 days. (−) indicated without NIR irradiation, and (+) indicated with NIR irradiation. Each experiment group has 6 mice (n = 6). Data are presented as the mean ± SD. n.s.: no significance, *p < 0.05, **p < 0.01, ***p < 0.001.

University of Chinese Academy of Sciences (approval WIUCAS21031002) and complied with the recommendations of the academy's animal research guidelines.

Declaration of competing interest

The authors declare that they have no known competing financial interests or personal relationships that could have appeared to influence the work reported in this paper.

CRediT authorship contribution statement

Qingfei Zhang: Conceptualization, Methodology, Investigation, Writing – original draft, Writing – review & editing, Funding acquisition. **Xiaocheng Wang:** Methodology, Investigation, Validation, Formal analysis, Writing – original draft. **Gaizhen Kuang:** Investigation, Data curation, Writing – review & editing. **Yuanjin Zhao:** Conceptualization, Writing – review & editing, Supervision, Funding acquisition.

Acknowledgments

This work was supported by the National Key Research and Development Program of China (2020YFA0908200), the National Natural Science Foundation of China (52103196 and 52073060), Guangdong Basic and Applied Basic Research Foundation (2021B1515120054), and the Shenzhen Fundamental Research Program (JCYJ20190813152616459 and JCYJ20210324133214038).

Appendix A. Supplementary data

Supplementary data to this article can be found online at https://doi.org/10.1016/j.bioactmat.2022.12.020.

References

[1] H. Sung, J. Ferlay, R.L. Siegel, M. Laversanne, I. Soerjomataram, A. Jemal, F. Bray, Global cancer statistics 2020: globocan estimates of incidence and mortality worldwide for 36 cancers in 185 countries, CA A Cancer J. Clin. 71 (3) (2021) 209–249.

[2] R.L. Siegel, K.D. Miller, H.E. Fuchs, A. Jemal, Cancer statistics, 2021, CA-Cancer, J. Clin. 71 (1) (2021) 7–33.
[3] B.A. Chabner, T.G. Roberts, Chemotherapy and the war on cancer, Nat. Rev. Cancer 5 (1) (2005) 65–72.
[4] H. Xu, M. Hu, M. Liu, S. An, K. Guan, M. Wang, L. Li, J. Zhang, J. Li, L. Huang, Nano-puerarin regulates tumor microenvironment and facilitates chemo-and immunotherapy in murine triple negative breast cancer model, Biomaterials 235 (2020), 119769.
[5] M. Liu, A.R. Khan, J. Ji, G. Lin, X. Zhao, G. Zhai, Crosslinked self-assembled nanoparticles for chemo-sonodynamic combination therapy favoring antitumor, antimetastasis management and immune responses, J. Contr. Release 290 (2018) 150–164.
[6] M. Liu, H. Du, A.R. Khan, J. Ji, A. Yu, G. Zhai, Redox/enzyme sensitive chondroitin sulfate-based self-assembled nanoparticles loading docetaxel for the inhibition of metastasis and growth of melanoma, Carbohydr. Polym. 184 (2018) 82–93.
[7] T.C. Johnstone, K. Suntharalingam, S.J. Lippard, The next generation of platinum drugs: targeted Pt(II) agents, nanoparticle delivery, and Pt(IV) prodrugs, Chem. Rev. 116 (5) (2016) 3436–3486.
[8] L. Kelland, The resurgence of platinum-based cancer chemotherapy, Nat. Rev. Cancer 7 (8) (2007) 573–584.
[9] Q. Zhang, G. Kuang, S. He, S. Liu, H. Lu, X. Li, D. Zhou, Y. Huang, Chain-shattering Pt(IV)-backboned polymeric nanoplatform for efficient CRISPR/Cas9 gene editing to enhance synergistic cancer therapy, Nano Res. 14 (3) (2020) 601–610.
[10] H. Xiao, L. Yan, E.M. Dempsey, W. Song, R. Qi, W. Li, Y. Huang, X. Jing, D. Zhou, J. Ding, X. Chen, Recent progress in polymer-based platinum drug delivery systems, Prog. Polym. Sci. 87 (2018) 70–106.
[11] Y. Li, Z. Wang, Y. Qi, Z. Tang, X. Li, Y. Huang, A red-light activatable and mitochondrion-targeting PtIV complex to overcome drug resistance, Chem. Commun. 58 (60) (2022) 8404–8407.
[12] Q. Zhang, G. Kuang, Y. Yu, X. Ding, H. Ren, W. Sun, Y. Zhao, Hierarchical microparticles delivering oxaliplatin and NLG919 nanoprodrugs for local chemo-immunotherapy, ACS Appl. Mater. Interfaces 14 (43) (2022) 48527–48539.
[13] W. Tao, X. Ji, X. Xu, M.A. Islam, Z. Li, S. Chen, P.E. Saw, H. Zhang, Z. Bharwani, Z. Guo, J. Shi, O.C. Farokhzad, Antimonene quantum dots: synthesis and application as near-infrared photothermal agents for effective cancer therapy, Angew. Chem. Int. Ed. 56 (39) (2017) 11896–11900.
[14] Y. Yi, M. Yu, C. Feng, H. Hao, W. Zeng, C. Lin, H. Chen, F. Lv, D. Zhu, X. Ji, L. Mei, M. Wu, W. Tao, Transforming “cold” tumors into “hot” ones via tumor-microenvironment-responsive siRNA micelleplexes for enhanced immunotherapy, Matter 5 (7) (2022) 2285–2305.
[15] H.L. Ma, W. Li, M. Wang, L.C. Varanda, J.R. Perussi, Y.S. Zhang, E. Carrilho, In vitro 3D malignant melanoma model for the evaluation of hypericin-loaded oil-in-water microemulsion in photodynamic therapy, Bio-Des. Manuf. 5 (4) (2022) 660–673.
[16] H. Xiang, L. Zhao, L. Yu, H. Chen, C. Wei, Y. Chen, Y. Zhao, Self-assembled organic nanomedicine enables ultrastable photo-to-heat converting theranostics in the second near-infrared biowindow, Nat. Commun. 12 (1) (2021) 1–12.
[17] W. Yue, L. Chen, L. Yu, B. Zhou, H. Yin, W. Ren, C. Liu, L. Guo, Y. Zhang, L. Sun, K. Zhang, H. Xu, Y. Chen, Checkpoint blockade and nanosonosensitizer-augmented noninvasive sonodynamic therapy combination reduces tumour growth and metastases in mice, Nat. Commun. 10 (1) (2019) 1–15.
[18] D. Gao, T. Chen, S. Chen, X. Ren, Y. Han, Y. Li, Y. Wang, X. Guo, H. Wang, X. Chen, Targeting hypoxic tumors with hybrid nanobullets for oxygen-independent synergistic photothermal and thermodynamic therapy, Nano-Micro Lett. 13 (1) (2021) 1–21.
[19] X. Shou, H. Zhang, D. Wu, L. Zhong, D. Ni, T. Kong, Y. Zhao, Y. Zhao, Antigen-presenting hybrid colloidal crystal clusters for promoting T cells expansion, Small 17 (14) (2021), 2006955.
[20] X. Shou, Y. Liu, D. Wu, H. Zhang, Y. Zhao, W. Sun, X. Shen, Black phosphorus quantum dots doped multifunctional hydrogel particles for cancer immunotherapy, Chem. Eng. J. 408 (2021), 127349.
[21] H. Zhang, Y. Liu, C. Chen, W. Cui, C. Zhang, F. Ye, Y. Zhao, Responsive drug-delivery microcarriers based on the silk fibroin inverse opal scaffolds for controllable drug release, Appl. Mater. Today 19 (2020), 100540.
[22] G. Ying, N. Jiang, C. Parra-Cantu, G. Tang, J. Zhang, H. Wang, S. Chen, N.P. Huang, J. Xie, Y.S. Zhang, Bioprinted injectable hierarchically porous gelatin methacryloyl hydrogel constructs with shape-memory properties, Adv. Funct. Mater. 30 (46) (2020), 2003740.
[23] Z. Yang, D. Gao, X. Guo, L. Jin, J. Zheng, Y. Wang, S. Chen, X. Zheng, L. Zeng, M. Guo, Fighting immune cold and reprogramming immunosuppressive tumor microenvironment with red blood cell membrane-camouflaged nanobullets, ACS Nano 14 (12) (2020) 17442–17457.
[24] M. Luo, D. Dorothy Winston, W. Niu, Y. Wang, H. Zhao, X. Qu, B. Lei, Bioactive therapeutics-repair-enabled citrate-iron hydrogel scaffolds for efficient post-surgical skin cancer treatment, Chem. Eng. J. 431 (2022), 133596.
[25] X. Shi, Y. Cheng, J. Wang, H. Chen, X. Wang, X. Li, W. Tan, Z. Tan, 3D printed intelligent scaffold prevents recurrence and distal metastasis of breast cancer, Theranostics 10 (23) (2020) 10652–10664.
[26] Q. Zhang, X. Wang, G. Kuang, Y. Yu, Y. Zhao, Photopolymerized 3D printing scaffolds with Pt(IV) prodrug initiator for postsurgical tumor treatment, 2022, Research (2022), 9784510.
[27] L. Yang, Y. Liu, L. Sun, C. Zhao, G. Chen, Y. Zhao, Biomass microcapsules with stem cell encapsulation for bone repair, Nano-Micro Lett. 14 (1) (2021) 1–12.
[28] X. Wang, Y. Yu, C. Yang, L. Shang, Y. Zhao, X. Shen, Dynamically responsive scaffolds from microfluidic 3D printing for skin flap regeneration, Adv. Sci. 9 (22) (2022), 2201155.
[29] X. Liu, Y. Yu, D. Liu, J. Li, J. Sun, Q. Wei, Y. Zhao, S.J. Pandol, L. Li, Porous microcapsules encapsulating β cells generated by microfluidic electrospray technology for diabetes treatment, NPG Asia Mater. 14 (1) (2022) 39.
[30] Z. Luo, J. Che, L. Sun, L. Yang, Y. Zu, H. Wang, Y. Zhao, Microfluidic electrospray photo-crosslinkable κ-carrageenan microparticles for wound healing, Eng. Reg. 2 (2021) 257–262.
[31] J. Aleman, T. Kilic, L.S. Mille, S.R. Shin, Y.S. Zhang, Microfluidic integration of regeneratable electrochemical affinity-based biosensors for continual monitoring of organ-on-a-chip devices, Nat. Protoc. 16 (5) (2021) 2564–2593.
[32] J. Wang, D. Huang, H. Yu, Y. Cheng, H. Ren, Y. Zhao, Developing tissue engineering strategies for liver regeneration, Eng. Reg. 3 (2022) 80–91.
[33] D. Huang, C. Zhao, B. Wen, X. Fu, L. Shang, W. Kong, Y. Zhao, Oxygen-carrying microfluidic microcapsules for enhancing chemo-sonodynamic therapy on patient-derived tumor organoid models, Chem. Eng. J. 435 (2022), 134871.
[34] R. Cheng, L. Jiang, H. Gao, Z. Liu, E. Mäkilä, S. Wang, Q. Saiding, L. Xiang, X. Tang, M. Shi, J. Liu, L. Pang, J. Salonen, J. Hirvonen, H. Zhang, W. Cui, B. Shen, H. A. Santos, A pH-responsive cluster metal-organic framework nanoparticle for enhanced tumor accumulation and antitumor effect, Adv. Mater. 34 (42) (2022), 2203915.
[35] H. Zhang, W. Cui, X. Qu, H. Wu, L. Qu, X. Zhang, E. Mäkilä, J. Salonen, Y. Zhu, Z. Yang, D. Chen, H.A. Santos, M. Hai, D.A. Weitz, Photothermal-responsive nanosized hybrid polymersome as versatile therapeutics codelivery nanovehicle for effective tumor suppression, Proc. Natl. Acad. Sci. USA 116 (16) (2019) 7744–7749.
[36] M. Liu, W. Song, L. Huang, Drug delivery systems targeting tumor-associated fibroblasts for cancer immunotherapy, Cancer Lett. 448 (2019) 31–39.
[37] Q. Zhang, G. Kuang, S. He, H. Lu, Y. Cheng, D. Zhou, Y. Huang, Photoactivatable prodrug-backboned polymeric nanoparticles for efficient light-controlled gene delivery and synergistic treatment of platinum-resistant ovarian cancer, Nano Lett. 20 (5) (2020) 3039–3049.
[38] J. Yu, X. He, Q. Zhang, D. Zhou, Z. Wang, Y. Huang, Iodine conjugated Pt(IV) nanoparticles for precise chemotherapy with iodine–Pt guided computed tomography imaging and biotin-mediated tumor-targeting, ACS Nano 16 (4) (2022) 6835–6846.
[39] Q. Zhang, G. Kuang, D. Zhou, Y. Qi, M. Wang, X. Li, Y. Huang, Photoactivated polyprodrug nanoparticles for effective light-controlled Pt(IV) and siRNA codelivery to achieve synergistic cancer therapy, J. Mater. Chem. B 8 (27) (2020) 5903–5911.
[40] S. He, C. Li, Q. Zhang, J. Ding, X.J. Liang, X. Chen, H. Xiao, X. Chen, D. Zhou, Y. Huang, Tailoring platinum(IV) amphiphiles for self-targeting all-in-one assemblies as precise multimodal theranostic nanomedicine, ACS Nano 12 (7) (2018) 7272–7281.
[41] Z. Wang, G. Kuang, Z. Yu, A. Li, D. Zhou, Y. Huang, Light-activatable dual prodrug polymer nanoparticle for precise synergistic chemotherapy guided by drug-mediated computed tomography imaging, Acta Biomater. 94 (2019) 459–468.
[42] S. Bian, L. Hao, X. Qiu, J. Wu, H. Chang, G.M. Kuang, S. Zhang, X. Hu, Y. Dai, Z. Zhou, An injectable rapid-adhesion and anti-swelling adhesive hydrogel for hemostasis and wound sealing, Adv. Funct. Mater. 32 (46) (2022), 2207741.
[43] B. He, J. Wang, M. Xie, M. Xu, Y. Zhang, H. Hao, X. Xing, W. Lu, Q. Han, W. Liu, 3D printed biomimetic epithelium/stroma bilayer hydrogel implant for corneal regeneration, Bioact. Mater. 17 (2022) 234–247.
[44] X. Wu, M. Zhou, F. Jiang, S. Yin, S. Lin, G. Yang, Y. Lu, W. Zhang, X. Jiang, Marginal sealing around integral bilayer scaffolds for repairing osteochondral defects based on photocurable silk hydrogels, Bioact. Mater. 6 (11) (2021) 3976–3986.
[45] M. Imran, W. Ayub, I.S. Butler, R. Zia ur, Photoactivated platinum-based anticancer drugs, Coord. Chem. Rev. 376 (2018) 405–429.
[46] S. Xu, X. Zhu, C. Zhang, W. Huang, Y. Zhou, D. Yan, Oxygen and Pt(II) self-generating conjugate for synergistic photo-chemo therapy of hypoxic tumor, Nat. Commun. 9 (1) (2018) 2053.
[47] S. Gao, Y. Liu, M. Liu, D. Yang, M. Zhang, K. Shi, Biodegradable mesoporous nanocomposites with dual-targeting function for enhanced anti-tumor therapy, J. Contr. Release 341 (2022) 383–398.
[48] Y. Ma, S. Tong, G. Bao, C. Gao, Z. Dai, Indocyanine green loaded SPIO nanoparticles with phospholipid-PEG coating for dual-modal imaging and photothermal therapy, Biomaterials 34 (31) (2013) 7706–7714.